Possibilities of Electron Beam Melting Technology: Titanium Processing

Michaela Fousova, Dalibor Vojtech
Department of Metals and Corrosion Engineering, Faculty of Chemical Technology, University of Chemistry and technology Prague, Technicka 5, 166 28 Prague 6 – Dejvice, Czech Republic. E-mail: fousovam@vscht.cz, vojtechd@vscht.cz

Nowadays, 3D printing of metallic materials is a hot topic in many industrial spheres as it provides a one-step production of very complex parts. The additive principle based on processing of powders or wires in many successive layers minimizes material losses and so production costs. It also ensures great control over built shapes exactly according to computer-designed models. The most available technology is Selective Laser Melting (SLM) that uses a laser beam to selectively melt a metallic powder into the form of a desired product. The Electron Beam Melting (EBM) technology, that is based on a similar principle, is not so widespread, especially in the Czech Republic. Instead of a laser beam, it uses an electron beam. Related to that, EBM is far more energy-efficient and has different process characteristics. In this contribution, on the example of titanium alloy, we show marginal possibilities of this technology in the processing of bulk materials, from porous to highly dense.

Keywords: EBM, electron beam melting, Ti6Al4V, mechanical properties

1 Introduction

Electron beam melting (EBM) belongs among techniques of Additive Manufacture (AM). We can often come across related synonyms such as 3D printing, solid free-form fabrication or rapid prototyping (although AM has already moved from prototyping to an actual production) too. AM is a rapidly developing technology that has the potential to revolutionize product development and fabrication in industries ranging from aerospace to medical. The layerwise process eliminates geometric constraints associated with traditional manufacturing processes and provides nearly complete design freedom. Novel complex geometries or even custom-tailored products thus become possible with AM [1]. Compared to common subctractive technologie, AM boasts with minimal material losses, short lead times and no tooling necessary as net-shape products are provided directly [2,3].

Several groups of AM processes are currently available depending on the type of an input material, heat source and the way of material supply [4]. SLM (selective laser melting) and EBM belong into the group of 'powder-bed' techniques. This term indicates that: 1. a powder material is processed and 2. it is deposited onto a work plate in many successive layers, thus forming a 'bed of powder'. This powder bed is then selectively melted by a laser or electron beam exactly according to the data from a computer 3D model [5]. While SLM production is already available in the Czech Republic, EBM is not yet.

Schema in Fig. 1 illustrates the arrangement of an EBM machine and its working principle. The arrangement is similar to a scanning electron microscope. An electron beam is generated by a tungsten filament and controlled by pairs of magnetic coils which determines the position, focus, shape and size of the beam. The electron beam is focused onto a powder bed to selectively melt the powder in coordinates given by a computer software based on thin virtual cuts through a CAD model. The software also allows to control beam current and parameters of the scanning process, such as scanning speed, distance between individual scan lines, number of scan repetitions, scanning pattern or rotation angle between consecutive scans [6]. EBM operation proceeds as follows: A heated tungsten filament emits electrons which are collimated and accelerated to a kinetic energy of about 6-60 keV. The beam current is controlled in the range of 1–50 mA and the beam diameter can be focused down to about 0.1 mm. In the middle part of the machine, a built chamber where the products are formed is situated. A metal powder is supplied from two hoppers and forms a thin layer (0.05–0.2 mm) on the base plate by a raking mechanism. Then, the computer-controlled electron beam scans over the powder layer and consolidates the desired areas into a solid and dense metal. After completing the melting in the first layer, the base plate is lowered, a new powder layer is deposited and the scanning process is repeated until all layers are finished [7].

In EBM, a vacuum is needed to avoid the deflection of an electron beam by gas molecules, whereas SLM process is conducted in an inert gas atmosphere. While powder particles directly absorb the heat energy from photons of a laser beam, in EBM, electrons penetrate into powder particles converting their kinetic energy into thermal energy to melt the powder. An electron beam has a more diffuse spot size than a focused laser spot. The larger spot size along with larger size of powder particles impede powder particles repelling each other due to charging by the electron beam. As a result, the minimum feature size, resolution and surface finish of EBM are typically larger than for SLM process. On the other hand, the EBM process is far more energy-efficient than the laser technology and the vacuum supports processing of reactive metals [8]. The use of an electron beam also allows preheating of a powder bed to reduce thermal gradients during the EBM process and thereby reduce internal stresses in final products. Usually, prior to an actual scanning of each layer, a pre-scan is carried out using high scanning speeds and high beam currents. Therefore, the powder heats up and pre-sinters but do not melt. Afterwards, actual scanning at lower speeds and currents

follows [9].

In this paper, we present the EBM technology applied on processing of titanium alloy Ti6Al4V. Using two regimes of strongly different parameters, we show marginal possibilities of this technology in preparation of bulk samples. The MELT regime exhibits the possibility to achieve nearly theoretical density. On the contrary, the NET regime represent the potential for weight reductions by introduction of random internal porosity.

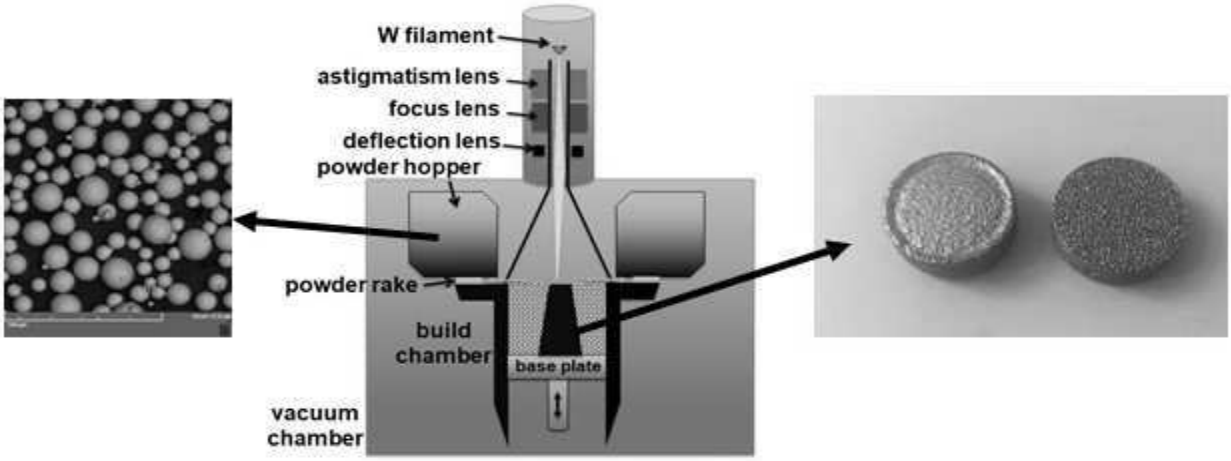

Fig. 1 *Schema of EBM*

2 Experimental

2.1 EBM process

Samples for this study were produced using an Arcam Q10 EBM machine (Arcam, Sweden). Two regimes designated as MELT and NET were applied. The MELT regime is intended for a complete melting of powder particles of an input material and their fusion into the form of high-density products. For that purpose, a sufficiently high voltage is applied. The aim of the NET regime is opposite - the preparation of porous structures. To avoid the complete melting of powder particles and achieve their sintering, an electron beam is generated at a one order lower voltage. In this work, voltages of 60 and 6 kV were used.

The consolidation of the input powder material was accomplished by continuous scanning of an electron beam across a powder bed. The process was repeated in many successive layers until final samples were completed. Layer thickness was set to 50 μm. The sintering/melting process was carried in an evacuated chamber (10^{-3} mbar) on a building plate preheated up to a temperature of 740 °C. Prior to actual melting, each layer was first preheated using a pre-scan with a beam current set to 30 mA and a speed of 10,000 mm s^{-1}.

In the MELT regime, a beam of 15 mA current was scanned in lines across areas intended to melt at a speed of 4,530 mm s^{-1}. Focused on the powder bed, the electron beam formed a scan track of 100 μm in size. The hatching space in between adjacent lines was set to 0.2 mm. In the NET regime, both values of scanning speed and beam current were lower (1500 mm s^{-1} and 3 mA, respectively), thus resulting in lower energy.

2.2 Material

A titanium alloy Ti6Al4V was selected for the purpose of this study as it represents one of the metallic materials most frequently processed by the additive manufacture. A powder of this alloy was purchased from a commercial supplier of metallic powders intended for AM (AP&C). The average particle size of this gas-atomized powder was 75 μm (45-105 μm).

Flat cylinders of 15 mm in diameter and 5 mm in height were fabricated by EBM (shown on the right image in Fig. 1). All samples were kept in the as-produced state, without any surface treatment.

2.3 Material characterization

Surface morphology of the as-produced samples was observed by a scanning electron microscope (SEM) TESCAN VEGA-3 LMU equipped with an Oxford instruments INCA 350 EDX analyzer. Both bottom and top surfaces were documented.

For microstructure observation, metallographic sections were prepared in longitudinal and transverse directions. Chemically-mechanically polished (silica suspension supplemented with 20 vol.% H_2O_2) sections were first subjected to porosity analysis and then etched Kroll's reagent. Porosity was evaluated on unetched samples by optical microscopy (OM, Olympus PME3) along with image analysis (ImageJ software). FeretX (parallel to the scanning direction) and FeretY (parallel to the building direction) diameters were used to determine the distribution of pore size. On etched samples, a microstructure was observed by OM and SEM. Phase composition was confirmed by X-ray diffraction using PANalytical X'Pert PRO diffractometer equipped with Cu anode.

Mechanical properties were evaluated under uniaxial compression using a LabTest 5.250SP1-VM universal loading machine. Cubes with a 5 mm edge length were cut out of the samples. The compression tests were carried out at room temperature with a strain rate of 0.001 s^{-1} in the direction parallel to the building direction. For statistical purposes, three specimens were measured. To evaluate the influence of microstructure within the grains,

Vicker's hardness HV0.5 was determined using a micro-hardness Future-Tech FM-700 tester.

3 Results and Discussion

3.1 Surface

Figure 2 shows a comparison between the macroscopic appearance of the MELT and NET samples. The top side of the MELT samples is smooth as the melt fused perfectly. The bottom side, that represents the first layer, is much uneven. In the first layer, the melt is in a direct contact with a loose powder. Therefore, many particles beneath are also partially melted and adhere to the layer bottom during its solidification. The surface of the NET is discontinuous as numerous pores pass through it. That is the consequence of a low energy used to melt the material. The melt in adjacent scan tracks do not fuse perfectly. As a result, pores remain in the structure. Also, some partially melted particles of the original powder can be observed. The bottom side of the NET samples is similar to the MELT samples, with only the difference of pores emerging on the surface.

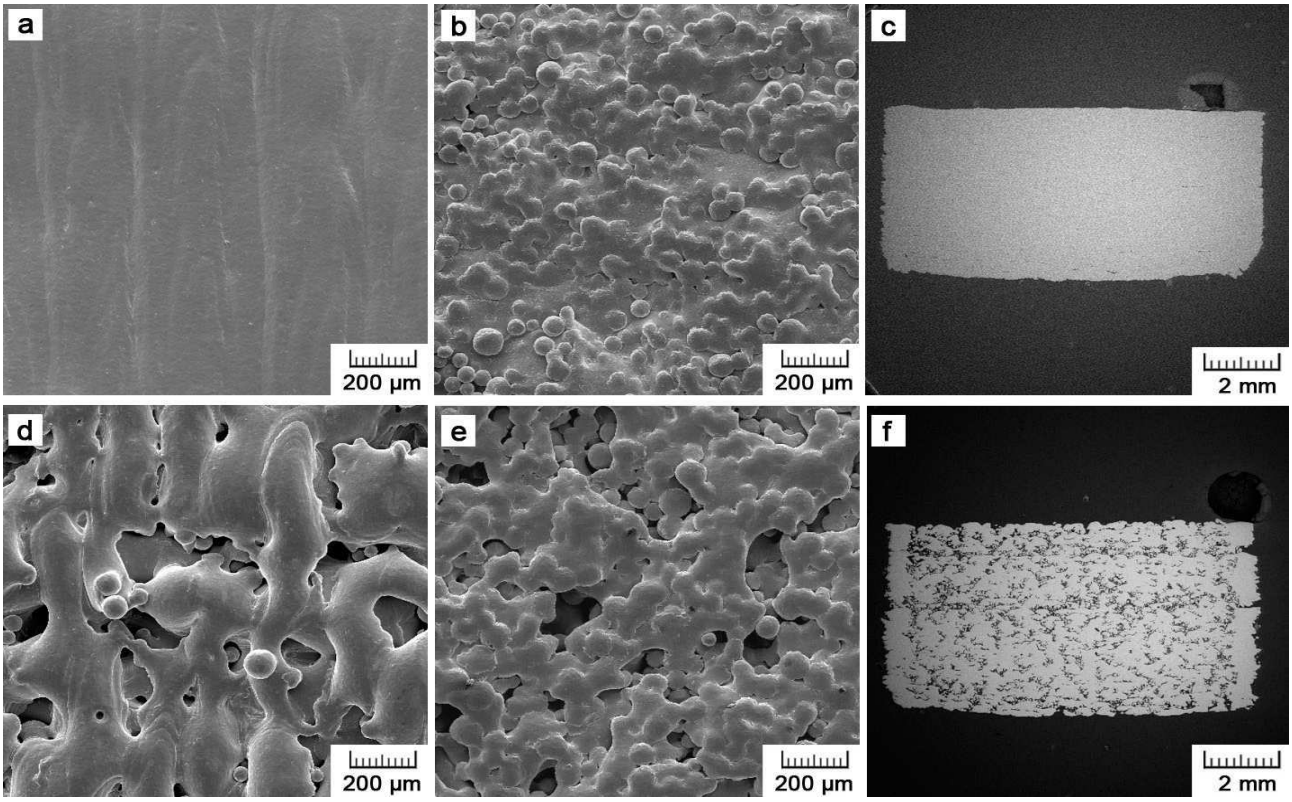

Fig. 2 *Top (a,d) and bottom (b,e) surfaces of MELT (a-c) and NET (d-f) samples along with longitudinal sections (c,d)*

3.2 Porosity

Images c and f in Fig. 2 bring longitudinal sections through the center of the samples. The difference in a porosity between the NET and MELT samples is obvious. The NET samples clearly shows a significant porosity. The total porosity was determined to be 29.8%. Compared to that, the MELT samples are perfectly dense, with minimal porosity in the first few layers. The total porosity is 0.5% here.

While the AM is mostly applied for the preparation of controlled porosity and precise porous structures [10-12], the NET regime of EBM provides random porosity. Histograms in Fig. 3 show the distribution of pore sizes (Feret's diameters parallel or perpendicular to the building direction) and areas. Based on values of FeretX overpassing those of FeretY, one can say that the pores are more elongated in the scanning direction in between adjacent scan tracks than in the building direction, across layers. About a half porosity (16.5%) is represented by pores of $10\text{-}200.10^3$ µm^2 in area.

Such titanium foams are possible to be used in a wide range of applications. Regarding the biocompatibility of Ti6Al4V alloy, simple augmentations for filling bone defects could be prepared. With an appropriate level of porosity, mechanical properties of bones can be matched to avoid stress-shielding effect and thinning of adjacent bone tissue. Open pores are also ideal for carrying biological agents or a bone substitute material to enhance the healing process [13,14]. Porous metals are also highly desired in aircraft and automotive industry. Not only the porosity reduces weight, but porous materials also exert higher impact toughness so can be used effectively as protective elements in impact areas of cars [15]. It is also well known that high-porosity sintered powder- or fiber-base materials possess higher vibration absorbing or damping properties as compared with bulk materials [16]. Additionaly, compared to conventional preparation methods of metallic foams (such as powder metallurgy, foaming etc.[17,18]), EBM, as an additive technology, offers the great advantage of producing net-shape products. Therefore, we can avoid part machining that might be often expensive, time-consuming and complicated, especially in the case of porous materials [19].

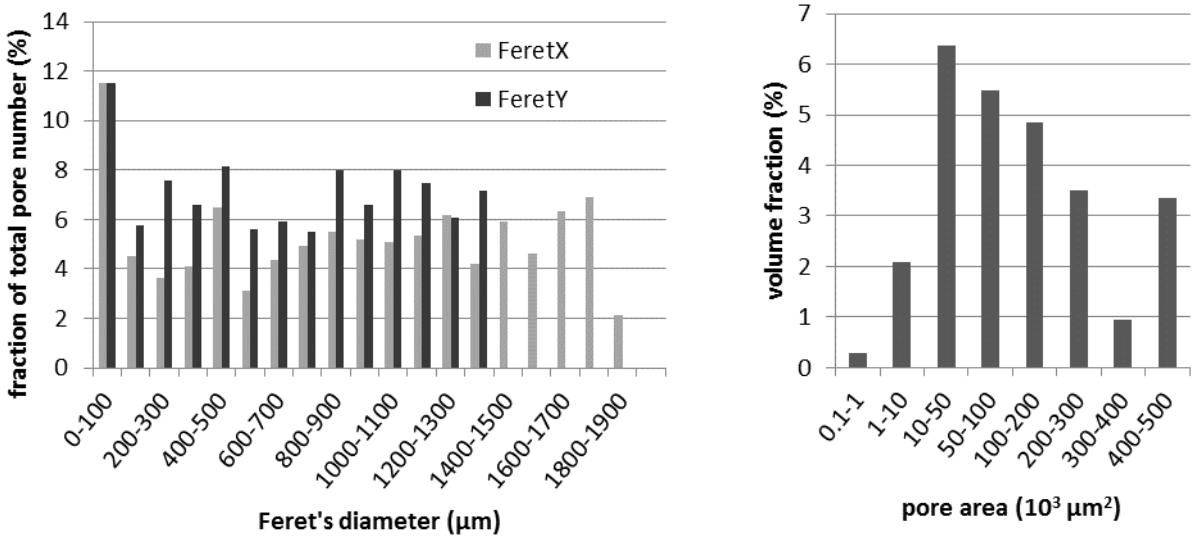

Fig. 3 *Porosity histograms*

3.3 Microstructure

In both types of samples, microstructure is formed by columnar grains elongated in the building direction. These are prior-β grains that transforms during solidification. Along with the melting of a particular layer, one or more previously solidified layers are reheated to a temperature higher than the β-transus and retransformed to the β phase. That results in an epitaxial growth of grains in the same crystallographic orientation as in previous layers [20].

In the MELT regime, a high-energy electron beam first creates a melt pool. Its temperature is estimated to about 2500 °C [21,22]. Then the melt pool solidifies, β-grains are formed and subsequently transformed. The transformation is controlled by the cooling rate from the solidification temperature (1900 °C) to the chamber temperature. Because the cooling rate is in the range of 10^3-10^5 °C/s [23] and the critical martensitic transformation cooling rate is estimated to 410 °C/s [24], α' martensite phase is formed by a diffussionless transformation. As the whole build chamber is kept at a higher temperature of the chamber (usually 650-750 °C), the solidified material dwells at this temperature during the rest of the whole EBM process. In this stage, martensitic phase transforms into a more stable α+β microstructure. The final stage comprises a slow cooling down to room temperature. Hovewer, the thermal history is more complex due to re-melting and re-heating of previously solidified layers [25]. Therefore, a lamellar mixture of α+β phases can be observed in Figs. 4b-c. The lamellae are very fine, with thickness below 1 µm. Boundaries of prior-β columnar grains can be distinguished due to a layer of α phase (Fig. 2b).

The situation in the NET regime is different. Martensitic needles remain in the final product. A mixed α+β microstructure along with martensitic needles can be observed in micrographs in Figs. 4e-f. However, in the bottom part of the samples α+β microstructure was observed (Figs. 4g-h). It is thus possible, that in the bottom part the cooling rate overcame the critical rate needed for martensitic transformation and martensite then decomposed at the temperature of 740 °C (higher than M_f = martensite finish [26]) to a mixture of α+β phases completely. However, in higher layers, presence of pores caused changes in thermal field. We assume following explanations: 1. The convection from the heated base plate through the solidified bulk was reduced by present voids. 2. Also, in areas below these voids, there was no repeated remelting and reheating by scanning electron beam in following layers. Both these pore manifestations led to a lower temperature at which the material was kept after solidification. Also the lower beam energy contributed to the lower temperature. The lower temperature then resulted in only partial decomposition of α′-martensite. It was already shown in previous studies of other authors [10,27] that in thin structures, α′-martensite may be present.

The difference in phase composition is also apparent from diffraction patterns in Fig. 4. It is not possible to distinguish α phase and α‘ martensite as both have hcp structure and differences in lattice parameters are only very small. However, presence of β phase in the MELT samples is evidenced by two peaks in the pattern. Low intensity of the peaks corresponds to the small amount of β phase in the microstructure. Although there is a minority amount of β phase in the NET samples too, it does not provide sufficient signal to give peaks in the spectrum.

One can also notice difference in thickness of prior-β grains. In the MELT samples, the grain thickness is below 50 µm (45±20 µm). In the NET samples, grains are thicker (90±30 µm). In ref. [28] the grains were shown to be thicker with wider melt pools. Wider melt pools can be attributed to lower speed and lower power of the beam in the NET régime [29]. Also, the presence of pores may contribute to reduced heat dissipation and longer persistence at a high temperature, which supports the growth of prior-β grains in thickness.

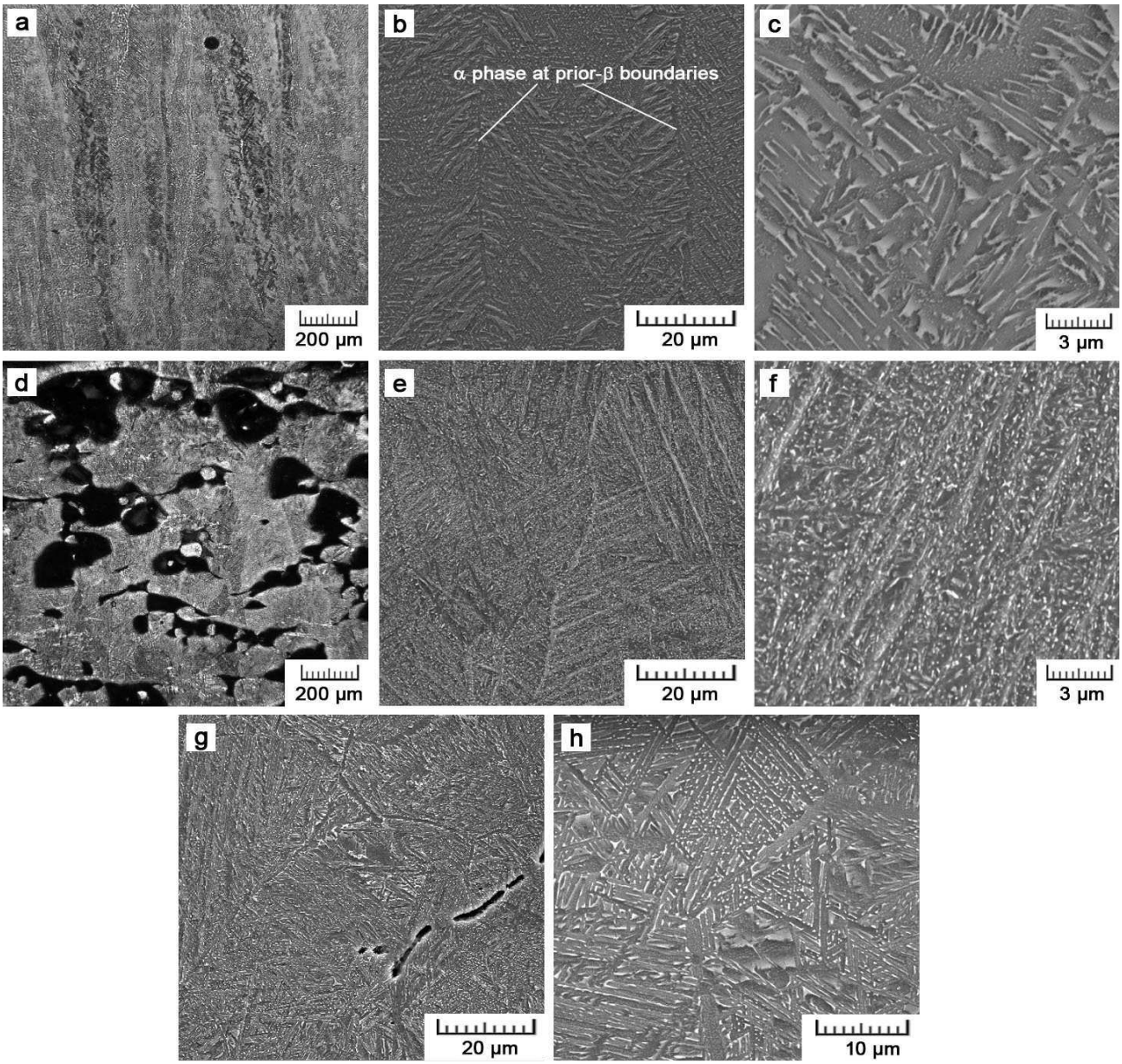

Fig. 4 *Microstructures of MELT (a-c) and NET (d-h) samples*

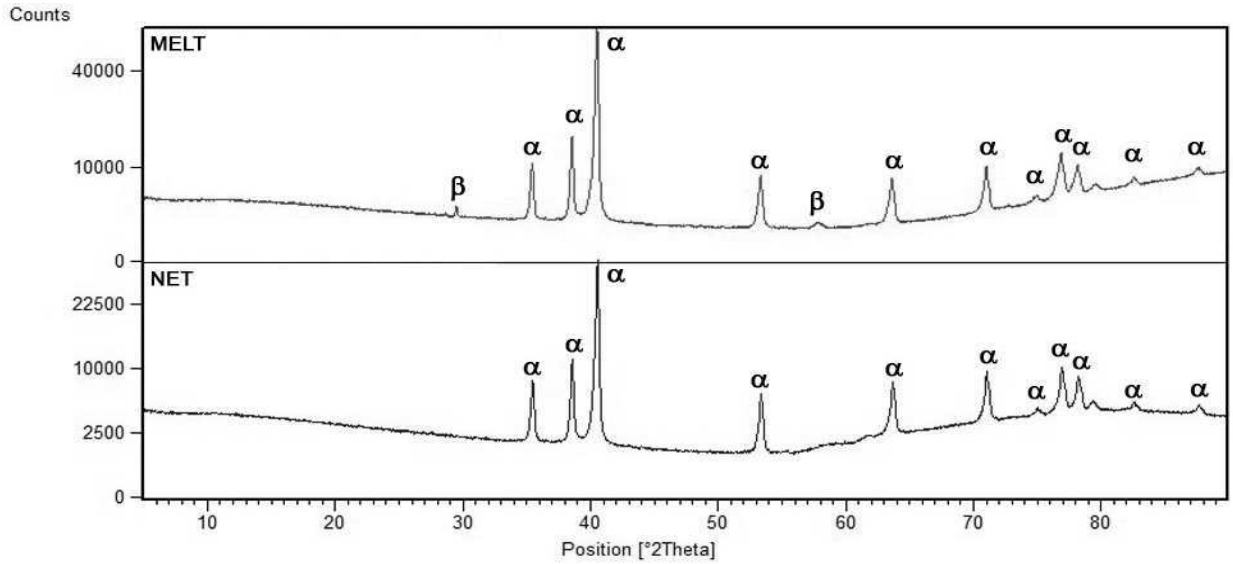

Fig. 5 *XRD patterns for MELT and NET samples*

3.4 Mechanical properties

The results of the hardness measurement corresponds to the observed microstructural features. The hardness of MELT samples reached a hardness of 386±6 HV0.5. A higher hardness of 422±10 HV0.5 was caused by very thin martensitic needles inside the grains of the NET samples. Tan et al. [30] even suggested to apply specific process parameters (e.g. low beam currents) to obtain a mixed α′ + α/β microstructure on purpose as it provides high strength and toughness.

Figure 6 shows a comparison of representing stress strain curves for the MELT and NET samples. Despite higher hardness, ultimate and yield strengths of the NET samples reached half the value of the MELT samples due to their significant porosity (for exact values consult Table 1).

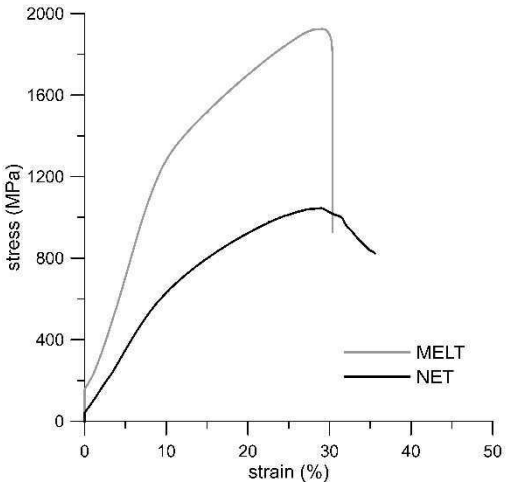

Fig. 6 *Representative tensile curves for different orientation of Ti6Al4V SLM samples*

Tab. 1 *Mechanical properties under compression (CYS =compressive yield strength, UCS = ultimate compressive strength, E = compressive modulus of elasticity, A = maximal strain)*

	CYS (MPa)	UCS (MPa)	E (GPa)	A_t (%)
MELT	1154±62	1870±77	14.2±0.4	15.3±2.5
NET	499±16	1033±19	7.0±0.1	not measurable

4 Conclusion

Our paper showed the possibilities of EBM at the example of processing Ti6Al4V alloy. The high-energy MELT regime resulted in a dense bulk material with density reaching a theoretical value. Conversely, by the low-energy NET regime, almost 30% porosity was achieved. The porosity led to a decrease in mechanical properties and also affected thermal history of the part influencing microstructure evolution.

Acknowledgement

Authors wish to thank the Czech Science Foundation (project no. P108/12/G043) and specific university research (MSMT No. 20-SVV/2017) for the financial support of this research. Thanks also MIRDC for providing the tested material.

References

[1] SEIFI, M., SALEM, A., SATKO, D., SHAFFER, J., LEWANDOWSKI, J. J. (2017). Defect distribution and microstructure heterogeneity effects on fracture resistance and fatigue behavior of EBM Ti–6Al–4V. In: *International Journal of Fatigue*, Vol. 94, pp. 263-287.

[2] FOUSOVÁ, M., VOJTĚCH, D., KUBÁSEK, J., DVORSKÝ, D., MACHOVÁ, M. (2015). 3D Printing as an Alternative to Casting, Forging and Machining Technologies? In: *Manufacturing Technology*, Vol. 15, No. 5, pp. 809-814.

[3] HERZOG, D., SEYDA, V., WYCISK, E., EMMELMANN, C. (2016). Additive manufacturing of metals. In: *Acta Materialia*, Vol. 117, pp. 371-392.

[4] FRAZIER, W. E. (2014). Metal Additive Manufacturing: A Review. In: *Journal of Materials Engineering and Performance*, Vol. 23, No. 6, pp. 1917-1928.

[5] ASTM INTERNATIONAL (2012). Standard terminology for additive manufacturing technologies. In: *ASTM Standard F2792-12a*.

[6] GALARRAGA, H., WARREN, R. J., LADOS, D. A., DEHOFF, R. R., KIRKA, M. M. (2017). Fatigue crack growth mechanisms at the microstructure scale in as-fabricated and heat treated Ti-6Al-4V ELI manufactured by electron beam melting (EBM). In: *Engineering Fracture Mechanics*, Vol. 176, pp. 263-280.

[7] GONG, X., ANDERSON, T., CHOU, K. (2014). Review on powder-based electron beam additive manufacturing technology. In: *Manufacturing Review*, Vol. 1, p. 2.

[8] HIEMENZ, J. (2007). Electron beam melting. In: *Advanced Materials and Processes*, Vol. 165, No. 3, pp. 45-46.

[9] KOIKE, M., GREER, P., OWEN, K., LILLY, G., MURR, L. E., GAYTAN, S. M., MARTINEZ, E., OKABE, T. (2011). Evaluation of Titanium Alloys Fabricated Using Rapid Prototyping Technologies—Electron Beam Melting and Laser Beam Melting. In: *Materials*, Vol. 4, No. 10, p. 1776.

[10] ATAEE, A., LI, Y., FRASER, D., SONG, G., WEN, C. (2018). Anisotropic Ti-6Al-4V gyroid scaffolds manufactured by electron beam melting (EBM) for bone implant applications. In: *Materials & Design*, Vol. 137, pp. 345-354.

[11] ČAPEK, J., MACHOVÁ, M., FOUSOVÁ, M., KUBÁSEK, J., VOJTĚCH, D., FOJT, J., JABLONSKÁ, E., LIPOV, J., RUML, T. (2016). Highly porous, low elastic modulus 316L stainless steel scaffold prepared by selective laser melting. In: *Materials Science and Engineering: C*, Vol. 69, pp. 631-639.

[12] FOUSOVÁ, M., VOJTĚCH, D., KUBÁSEK, J., JABLONSKÁ, E., FOJT, J. (2017). Promising characteristics of gradient porosity Ti-6Al-4V alloy prepared by SLM process. In: *Journal of the Mechanical Behavior of Biomedical Materials*, Vol. 69, pp. 368-376.

[13] WU, S., LIU, X., YEUNG, K. W. K., LIU, C., YANG, X. (2014). Biomimetic porous scaffolds for bone tissue engineering. In: *Materials Science and Engineering: R: Reports*, Vol. 80, pp. 1-36.

[14] FOUSOVA, M., VOJTECH, D., JABLONSKA, E., FOJT, J., LIPOV, J. (2017). Novel Approach in the Use of Plasma Spray: Preparation of Bulk Titanium for Bone Augmentations. In: *Materials*, Vol. 10, No. 9, p. 987.

[15] QIN, J., CHEN, Q., YANG, C., HUANG, Y. (2016). Research process on property and application of metal porous materials. In: *Journal of Alloys and Compounds*, Vol. 654, pp. 39-44.

[16] LUGOVSKOI, Y. F., CHERNYSHEV, L. I. (2006). Damping properties of sintered high-porosity materials based on powders and discrete copper fibers. In: *Powder Metallurgy and Metal Ceramics*, Vol. 45, No. 11, pp. 599-604.

[17] SALVETR, P., NOVÁK, P., VOJTĚCH, D. (2013). Magnesium alloys for implants. In: *Manufacturing Technology*, Vol. 13, No. 3, pp. 395-399.

[18] KNAISLOVÁ, A., PETERKA, M., NOVÁK, P., VOJTĚCH, D. (2013). Porous Ti-Si alloys for implants. In: *Manufacturing Technology*, Vol. 13, No. 3, pp. 330-333.

[19] DEBROY, T., WEI, H. L., ZUBACK, J. S., MUKHERJEE, T., ELMER, J. W., MILEWSKI, J. O., BEESE, A. M., WILSON-HEID, A., DE, A., ZHANG, W. (2018). Additive manufacturing of metallic components – Process, structure and properties. In: *Progress in Materials Science*, Vol. 92, pp. 112-224.

[20] MORITA, T., TSUDA, C., NAKANO, T. (2017). Influences of scanning speed and short-time heat treatment on fundamental properties of Ti-6Al-4V alloy produced by EBM method. In: *Materials Science and Engineering: A*, Vol. 704, pp. 246-251.

[21] CHENG, B., PRICE, S., LYDON, J., COOPER, K., CHOU, K. (2014). On Process Temperature in Powder-Bed Electron Beam Additive Manufacturing: Model Development and Validation. In: *Journal of Manufacturing Science and Engineering*, Vol. 136, No. 6, p. 061018.

[22] SAFDAR, A., WEI, L. Y., SNIS, A., LAI, Z. (2012). Evaluation of microstructural development in electron beam melted Ti-6Al-4V. In: *Materials Characterization*, Vol. 65, pp. 8-15.

[23] AL-BERMANI, S. S., BLACKMORE, M. L., ZHANG, W., TODD, I. (2010). The origin of microstructural diversity, texture, and mechanical properties in electron beam melted Ti-6Al-4V. In: *Metallurgical and Materials Transactions A: Physical Metallurgy and Materials Science*, Vol. 41, No. 13, pp. 3422-3434.

[24] AHMED, T., RACK, H. J. (1998). Phase transformations during cooling in α + β titanium alloys. In: *Materials Science and Engineering A*, Vol. 243, No. 1-2, pp. 206-211.

[25] GALARRAGA, H., WARREN, R. J., LADOS, D. A., DEHOFF, R. R., KIRKA, M. M., NANDWANA, P. (2017). Effects of heat treatments on microstructure and properties of Ti-6Al-4V ELI alloy fabricated by electron beam melting (EBM). In: *Materials Science and Engineering: A*, Vol. 685, pp. 417-428.

[26] GIL MUR, F. X., RODRÍGUEZ, D., PLANELL, J. A. (1996). Influence of tempering temperature and time on the α′-Ti-6Al-4V martensite. In: *Journal of Alloys and Compounds*, Vol. 234, No. 2, pp. 287-289.

[27] LI, S. J., MURR, L. E., CHENG, X. Y., ZHANG, Z. B., HAO, Y. L., YANG, R., MEDINA, F., WICKER, R. B. (2012). Compression fatigue behavior of Ti–6Al–4V mesh arrays fabricated by electron beam melting. In: *Acta Materialia*, Vol. 60, No. 3, pp. 793-802.

[28] NARRA, S. P., CUNNINGHAM, R., BEUTH, J., ROLLETT, A. D. (2018). Location specific solidification microstructure control in electron beam melting of Ti-6Al-4V. In: *Additive Manufacturing*, Vol. 19, pp. 160-166.

[29] ANDREW, J. P., LIN, L. (2004). Modelling the geometry of a moving laser melt pool and deposition track via energy and mass balances. In: *Journal of Physics D: Applied Physics*, Vol. 37, No. 14, p. 1885.

[30] TAN, X., KOK, Y., TOH, W. Q., TAN, Y. J., DESCOINS, M., MANGELINCK, D., TOR, S. B., LEONG, K. F., CHUA, C. K. (2016). Revealing martensitic transformation and α/β interface evolution in electron beam melting three-dimensional-printed Ti-6Al-4V. In: *Scientific Reports*, Vol. 6, p. 26039.

10.21062/ujep/110.2018/a/1213-2489/MT/18/3/387